Buckling and crush resistance of high-density TRIP-steel and TRIP-matrix composite honeycombs to out-of-plane compressive load

D. Ehinger [a,*], L. Krüger [a], U. Martin [a], C. Weigelt [b], C.G. Aneziris [b]

[a] Institute of Materials Engineering, Technische Universität Bergakademie Freiberg, Germany
[b] Institute of Ceramics, Glass and Construction Materials, Technische Universität Bergakademie Freiberg, Germany

ABSTRACT

The mechanical and structural responses of high-density TRIP steel and TRIP-steel/zirconia composite honeycomb structures were studied under uniaxial compression in the out-of-plane loading direction over a wide range of strain rates. Their mechanical response, buckling, and failure mechanisms differ considerably from those of conventional thin-walled, low-density cellular structures. Following the linear-elastic regime and the yield limit of the bulk material, the high-density square honeycombs exhibited a uniform increase in compression stress over an extended range of (stable) plastic deformation. This plastic pre-buckling stage with axial crushing of cell walls correlates with the uniaxial compressive response of the bulk specimens tested. The dominating material effects were the pronounced strain hardening of the austenitic steel matrix accompanied by a strain-induced α′-martensite nucleation (TRIP effect) and the strengthening effect due to the zirconia particle reinforcement. The onset of critical plastic bifurcation was initiated at high compressive loads governed by local or global cell wall deflections. After exceeding the compressive peak stress (maximum loading limit), the honeycombs underwent either a continuous post-buckling mode with a folding collapse (lower relative density) or a symmetric extensional collapse mode of the entire frame (high relative density). The densification strain and the post-buckling or plateau stress were determined by the energy efficiency method. Apart from relative density, the crush resistance and deformability of the honeycombs were highly influenced by the microstructure and damage evolution in the cell walls as well as the bulk material's strain-rate sensitivity. A significant increase in strain rate against quasi-static loading resulted in a measured enhancement of deformation temperature associated with material softening. As a consequence, the compressive peak stress and the plastic failure strain at the beginning of post-buckling showed an anomaly with respect to strain rate indicated by minimum values under medium loading-rate conditions. The development of the temperature gradient in the stable pre-buckling stage could be predicted well by a known constitutive model for quasi-adiabatic heating.

© 2015 The Authors. Published by Elsevier Ltd. This is an open access article under the CC BY license (http://creativecommons.org/licenses/by/4.0/).

1. Introduction

In recent decades, fundamental topics such as the potential for light-weight applications, crashworthiness, and passive safety have dictated the field of engineering in the civil and military transportation industries. Most of the crash-absorbing concepts applied on front and side bumpers in vehicle bodies or on crash barriers for offshore structures and oil tankers (Alghamdi, 2001) refer to thin-walled, metal-based structures and cellular materials which are able to convert a high degree of kinetic impact energy into plastic deformation energy. Their crush resistance and mode of collapse or failure are significantly influenced by loading direction and impact velocity, as well as by structural and material design.

Pioneering work on the mechanical properties of cellular materials and the prediction of their deformation mechanics is described in the literature (Gent and Thomas, 1963; Patel and Finnie, 1970; Shaw and Sata, 1966). The mechanical response of cellular structures like metal foams or honeycombs is controlled by their relative density $\bar{\rho}$ (the fraction of space occupied by the solid), cell size, and wall thickness as well as by the cell morphology and geometric irregularities (Gibson and Ashby, 1997; Gong and Kyriakides, 2005; Gong et al., 2005; Jang and Kyriakides, 2009a,b). Thus, most open-cell foams and two-dimensional periodic cellular structures with hexagonal, diamond, or square cell shapes that are compressed in-plane obliquely to the longitudinal axis of the cell walls (denoted as the X_1 or X_2 loading direction) behave as kinematically

* Corresponding author. Tel.: +49 3731 39 2766.
E-mail address: David.Ehinger@iww.tu-freiberg.de (D. Ehinger).

compliant mechanisms or bending-dominated materials (Papka and Kyriakides, 1994; Warren and Kraynik, 1987). After following a nearly linear elastic regime, they develop a maximum loading limit which corresponds to the onset of buckling-type instability (Triantafyllidis and Schraad, 1998). As a consequence, local distortion and rotation of cells is initiated, inducing either uniform cell crushing in a symmetrical and/or an asymmetrical manner or localization of deformation in discrete bands (Klintworth and Stronge, 1988, 1989; Papka and Kyriakides, 1994, 1998a,b; Prakash et al., 1996; Shim and Stronge, 1986). By contrast, the out-of-plane stiffness and strength of honeycombs are much higher because the cell walls undergo a stretch-dominated deformation mode involving large membrane compressions and extensions.

The majority of publications (Foo et al., 2007; Heimbs et al., 2007; Wilbert et al., 2011; Zhang and Ashby, 1992; Zhou and Mayer, 2002) focus on the crush behavior of thin-walled hexagonal aluminum or nomex honeycombs commonly produced by a sheet corrugation or expansion process. Their out-of-plane compressive response is characterized by initial stable elastic deformation of the cell walls before initiating a local flexural buckling at the onset of instability (López Jiménez and Triantafyllidis, 2013). The maximum load indicates the beginning of the folding collapse mode directly followed by intermediate softening of the structure. Further compressive deformation leads to a progressive collapse mechanism with the formation of multiple folds. Similarly to in-plane loading, an extended stress plateau can be observed. The folding process in metallic honeycombs is characterized by extensive plastic bending, rolling, and membrane deformations and is simultaneously accompanied by the localization of deformation in narrow collapse bands (McFarland, 1963; Mohr and Doyoyo, 2003, 2004; Wierzbicki, 1983).

The characterization of strain-rate sensitivity and dynamic crushing response of cellular structures at typical nominal strain rates in the range of $10^2 \text{ s}^{-1} \leqslant \dot{\varepsilon} \leqslant 10^5 \text{ s}^{-1}$ has already been carried out by a large number of research groups using drop weight tower apparatuses (Heimbs et al., 2007; Yamashita and Gotoh, 2005), Hopkinson pressure bar devices (Barnes et al., 2014; Elnasri et al., 2007; Pattofatto et al., 2007; Radford et al., 2007; Reid and Peng, 1997; Tan et al., 2005a,b; Zhao and Gary, 1998), Taylor anvil test fixtures (Baker et al., 1998; Goldsmith and Louie, 1995; Rathbun et al., 2006) and explosive test techniques (Dharmasena et al., 2008; Wadley et al., 2007), often in combination with high-speed photography. Altogether, four basic characteristics indicate the strain-rate sensitivity of cellular structures, including the intrinsic or inherent strain-rate sensitivity of the cell wall matrix material, the increase of pressure because of entrapped fluid in the cells, the inertia effect, and strengthening due to plastic-wave or shock-wave propagation (Gaitanaros and Kyriakides, 2014; Reid and Peng, 1997; Zhao and Abdennadher, 2004; Zhao et al., 2005). Depending on the cell wall matrix material, the cell morphology, the relative density, and the applied impact velocity, a dynamic enhancement of the initial peak load and the plateau stress can occur.

However, the majority of publications mentioned above have one thing in common. Their experimental and numerical investigations were focused on low-density cellular structures with relative densities of between 0.02 and 0.1. Hence, a limited amount of literature has been published that deals with the out-of-plane compressive behavior of high-density metallic honeycombs (Baker et al., 1998; Côté et al., 2004, 2006; Lu and Hinnerichs, 2001; Radford et al., 2007; Wadley et al., 2007; Wang et al., 2005). These research groups have already shown that prismatic or corrugated high-density honeycombs (relative density $\bar{\rho} > 0.1$) made from high-strength metal alloys or high strain-hardening stainless steels are promising for applications in automobile crash

absorbers, in blast-resistant sandwich plates for shock mitigation, or as armor materials for personnel carriers. In high-density metallic honeycombs, plastic cell wall buckling and plastic yielding near the cell nodes and edges are the dominant deformation mechanisms before the beginning of post-buckling collapse.

With regard to the present study, the cell wall matrix material of the square honeycombs consisted of high-alloyed austenitic AISI 304 CrNi steel with or without reinforcement by zirconia particles partially stabilized by MgO (Mg-PSZ). The increase in strength due to the strain-induced α'-martensite formation in the steel matrix (viz. the Transformation Induced Plasticity, or 'TRIP' effect) and the deformation constraints imposed by the embedded ceramic particles make important contributions to the honeycomb's crush resistance and energy absorption capability (Aneziris et al., 2009; Ehinger et al., 2012a, 2011, 2012b; Krüger et al., 2010).

This research work focuses on the stress–strain behavior of these square TRIP steel and TRIP-matrix composite honeycombs under out-of-plane (OOP) compression over a wide range of strain rates. Of particular interest is the buckling and post-buckling behavior that governs their strength and energy absorption. Two honeycombs of different relative densities were investigated. Their compressive stress–strain responses were correlated with the uniaxial response of the bulk material processed in the same manner using the same powder feedstock. In this regard, the influences of strain rate and Mg-PSZ content (0, 5 and 10 vol.%) on the mechanical properties and deformation mechanisms were considered. Infrared thermography was used during the compression experiments to enable in situ recording of failure and temperature. The temperature evolution was further described by a modified constitutive model for quasi-adiabatic heating (Meyer et al., 2007).

2. Material and methods

The honeycombs presented were fabricated by a modified ceramic extrusion technology which, unlike the common sheet corrugation, expansion, and slotting techniques, provides higher design flexibility and does not require additional joining processes (Baker et al., 1998; Côté et al., 2004, 2006). The powder feedstock consisted of an austenitic AISI 304 CrNi steel with different particle fractions of Mg-PSZ. It was processed to a plastic paste using certain powder mixing and blending steps (Weigelt et al., 2011). After plastic molding in a de-airing single-screw extruder with vacuum chamber, successive drying and debindering processes followed. The final pressure-less sintering was carried out at 1350 °C for 2 h in a 99.999% argon atmosphere.

The experimental test series were performed on sintered bulk materials and square honeycombs made from pure TRIP steel (denoted as 0Z, Fig. 1a) and two TRIP-matrix composite materials consisting of 5 and 10 vol.% zirconia (5Z or 10Z, Fig. 1b). Their chemical data with regard to the compositions of the sintered TRIP-steel matrices and the Mg-PSZ ceramic powder are given in Tables 1 and 2, respectively.

Two regular square honeycombs (cubed specimen, edge length of 8 mm) with an in-plane array of 4×4 (viz. 196 cells per square inch) and 2×2 closed cells (64 cpsi) denoted by a different average wall thickness and cell size were deformed under quasi-static compression in the out-of-plane loading direction X_3 (Fig. 2a). Additionally, the former higher-density honeycomb structure was subjected to compressive loads at various strain rates in the range of $10^{-3} \leqslant \dot{\varepsilon} \leqslant 1.9 \times 10^3 \text{ s}^{-1}$. Except for the dynamic impact tests in a Split-Hopkinson Pressure Bar (SHPB), larger specimens with a cross-section of 14×14 square cells (196 cpsi) and retained outer skin were used (Fig. 2b). These specimens ensured an accurate temperature measurement during deformation at medium strain rates. A further honeycomb geometry with 8×8 cells (64 cpsi)
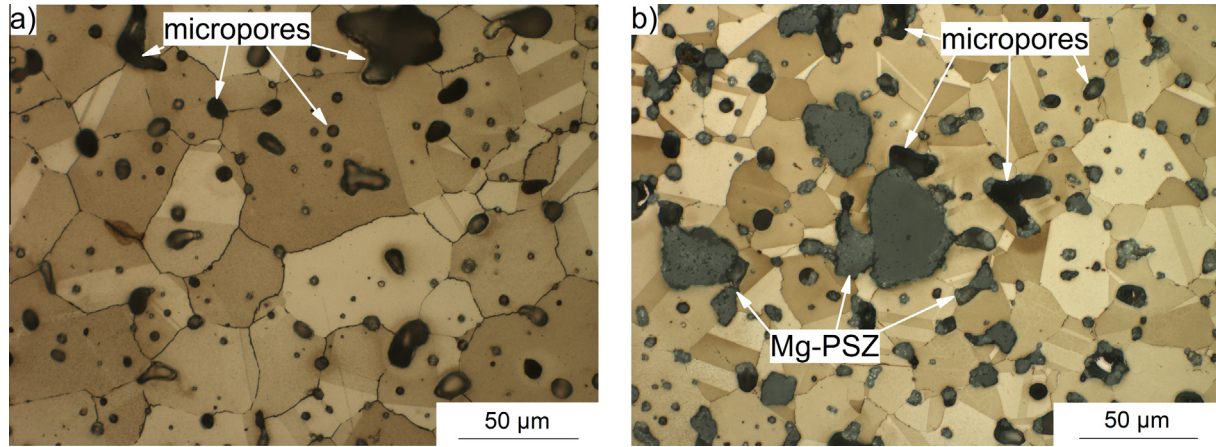
Fig. 1. Cell wall microstructure as-sintered: (a) pure TRIP steel (0Z), (b) TRIP-matrix composite with 10 vol.% Mg-PSZ (10Z); austenitic matrix with annealing twins is brown colored after Beraha II etching.

Table 1
Alloy compositions (in wt%) of the steel matrices in the bulk and honeycomb materials.

	C	Cr	Ni	Mn	Si	Fe and others
(a) Bulk materials:						
0Z	0.045	19.43	11.06	1.47	0.52	Bal.
5Z	0.044	18.71	10.47	1.38	0.50	Bal.
10Z	0.048	18.02	10.13	1.32	0.49	Bal.
(b) Honeycomb materials:						
0Z	0.042	18.60	9.25	0.92	0.53	Bal.
5Z	0.060	17.80	9.07	1.03	0.56	Bal.
10Z	0.068	17.40	8.80	1.00	0.53	Bal.

Table 2
Chemical analysis (in wt%) of the Mg-PSZ powder.

MgO	SiO_2	HfO_2	Al_2O_3	TiO_2	Na_2O	Fe_2O_3	ZrO_2
2.82	0.41	1.74	0.38	0.13	0.10	0.13	Bal.

and the same sample size was tested under quasi-static compression in order to investigate any possible scale effect.

The relative density $\bar{\rho}$ of two-dimensional multi-cell square columns is calculated by the ratio of global structure density ρ^* to material density ρ_s

$$\bar{\rho} = \left(\frac{\rho^*}{\rho_s}\right) = \frac{A}{A^*} \cong 2\frac{t}{l}, \tag{1}$$

where A and A^* describe the cross-sectional area of the bulk material and the global cross-sectional area of the honeycomb lattice ($A^* = b^2$), respectively. Due to processing, the effective (average) relative density $\bar{\rho}_{eff}$ of the presented honeycombs is significantly reduced by a varying volume content of microporosity p_m (maximum of 15 vol.%):

$$\bar{\rho}_{eff} = 2\frac{t}{l}(1 - p_m). \tag{2}$$

The mechanical properties of the corresponding bulk materials were determined under quasi-static uniaxial tensile loading ($\dot{\varepsilon} = 10^{-3} \, s^{-1}$) as well as uniaxial compressive loading at different strain rates in the range of $10^{-3} \, s^{-1}$ and $2.5 \times 10^3 \, s^{-1}$. The compression test series at quasi-static and medium strain rates ($\dot{\varepsilon} \leqslant 10^0 \, s^{-1}$) were performed using a servo-hydraulic universal testing machine of type MTS 880. For the tensile tests a universal testing machine of type Zwick 1476 was used. Dynamic impact and high strain-rate testing was carried out in an instrumented

drop weight tower (drop weight of approximately 190 kg and maximum drop height of 1 m, see Fig. 3a) and a Split-Hopkinson Pressure Bar (made of maraging steel X3CrNiCoMoTi8-9-5, bar diameter 19.8 mm, see Fig. 3b). The applied impact or striker velocity was $4 \, ms^{-1}$ for the drop weight tower and $15.5 \, ms^{-1}$ for the SHPB apparatus. The SHPB test setup ensured a stress-state equilibrium in the specimens (between the front and rear faces), a constant nominal strain rate, and a honeycomb deformation of up to 50%. More information about high strain rate testing on high-density square honeycombs is given in (Ehinger et al., 2012a). Furthermore, interrupted test runs were applied to study the buckling and failure evolution of the honeycombs in different deformation stages. In the case of dynamic impact testing, this was done by using rigid hollow cylinders of different height between the impact plates (cf. Fig. 3b). For each material and loading condition, at least five specimens were tested.

All information about the specimen type, its geometrical dimensions and the applied loading conditions is listed in Table 3.

The in situ recording of temperature and failure during compression was carried out using an FLIR ThermaCam S65 HS infrared device with a measuring accuracy of ±2 °C. The honeycomb specimens were therefore painted matt black to ensure maximum emissivity.

3. Results and discussion

3.1. Mechanical behavior of the bulk material

The flow curves of the powder metallurgical bulk specimens determined under quasi-static tensile and compressive loading ($\dot{\varepsilon} = 1 \times 10^{-3} \, s^{-1}$) are displayed in Fig. 4 with respect to the Mg-PSZ content. As already known from previous publications (Ehinger et al., 2011, 2012b; Krüger et al., 2011), the work-hardening behavior of the TRIP-matrix composite materials is driven by the dislocation processes and martensitic phase transformations in the austenitic steel, as well as by the deformation constraint effects originating from the embedded zirconia ceramic. Particle reinforcement is responsible for the increase in stress levels of the composites, ranging from plastic yield strain to a certain point of deformation. Since the degree of strengthening associated with the strain hardening of the austenitic steel matrix and the constraint effects of the zirconia particles is significantly influenced by the stress state, no uniform tensile/compressive deformation can be expected. If the composites are subjected to uniaxial compression, dislocation and martensite generation is favored in the interface
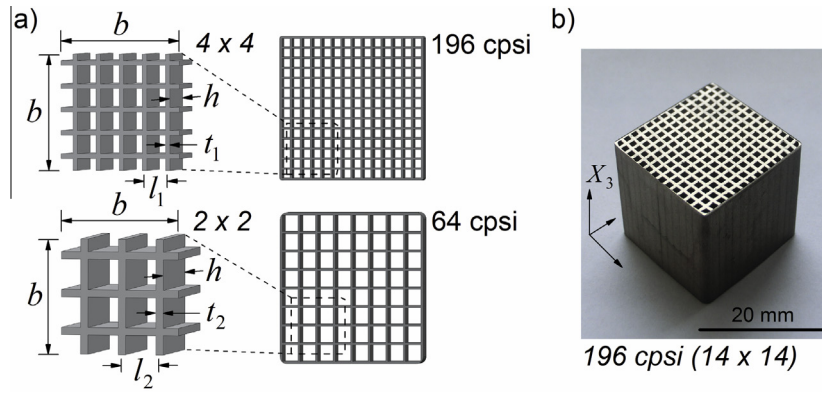
Fig. 2. Honeycomb geometries: (a) quasi-static test specimens dimensioned, (b) .14 × 14 (196 cpsi) honeycomb sample for various strain rate tests (here: X_3 denotes the OOP loading axis).
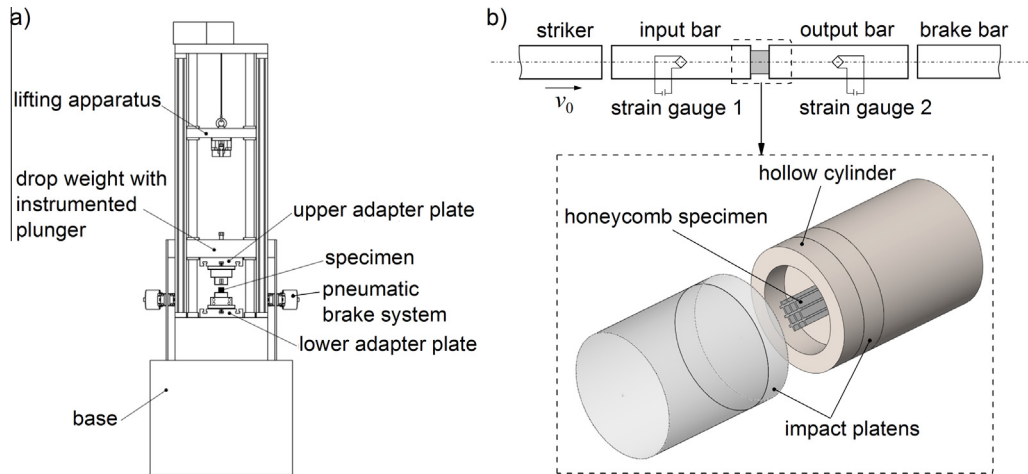

Fig. 3. Dynamic impact devices: (a) instrumented drop weight tower, (b) SHPB setup.

Table 3
Specimen dimensions and test parameters.

Sample geometry	t_1 or t_2 [mm]	l_1 or l_2 [mm]	b [mm]	h [mm]	$\bar{\rho}$ (Eq. (1)) [–]	$\vec{\rho}_{eff}$ (Eq. (2)) [–]	$\dot{\varepsilon}$ [s^{-1}]
(a) Honeycomb (small)							
64 cpsi (2 × 2)	0.30	2.4	8	8	0.25	0.235	1×10^{-3}
							1.9×10^3
196 cpsi (4 × 4)	0.32	1.5	8	8	0.43	0.362	1×10^{-3}
							1.9×10^3
(b) Honeycomb (large) with outer skin							
64 cpsi (8 × 8)	0.30	2.4	22	22	0.25	0.235	1×10^{-3}
196 cpsi (14 × 14)	0.32	1.5	22	22	0.43	0.362	1×10^{-3}
							$..1.9 \times 10^2$
	(Gauge) length [mm]		(Gauge) diameter [mm]			Cross-section	$\dot{\varepsilon}$ [s^{-1}]
(c) Bulk specimens							
Tensile	30		6			Circular	1×10^{-3}
Compressive	6		6			Circular	1×10^{-3}
							$..2.5 \times 10^3$

region at the poles of axially loaded ceramic particles (Martin et al., 2011). Under tensile loading, the contribution of Mg-PSZ to the strengthening of the material is inhibited by premature micro-failure. The typical features of damage are interface debonding, particle cracking, crack propagation through zirconia clusters, and the coalescence of micro-pores (Ehinger et al., 2011, 2012b).

Therefore, the composites exhibited a lower strength and ductility under quasi-static tensile loading (Fig. 4a), but outperformed the pure matrix material under compressive loading up to large degrees of deformation (Fig. 4b).

The effective tensile strain hardening or tangent modulus E_t of the bulk materials examined at 2% plastic strain
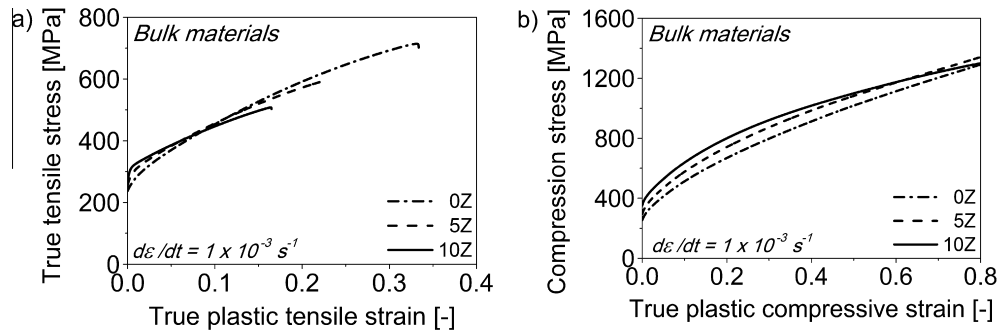
Fig. 4. Quasi-static flow curves of the TRIP steel (0Z) and TRIP-matrix composite (5Z, 10Z) bulk materials, (a) under uniaxial tensile and (b) compressive loading ($\dot{\varepsilon} = 1 \times 10^{-3}$ s^{-1}).

Table 4
Properties of the bulk materials for quasi-static tension and compression ($\dot{\varepsilon} = 1 \times 10^{-3}$ s^{-1}).

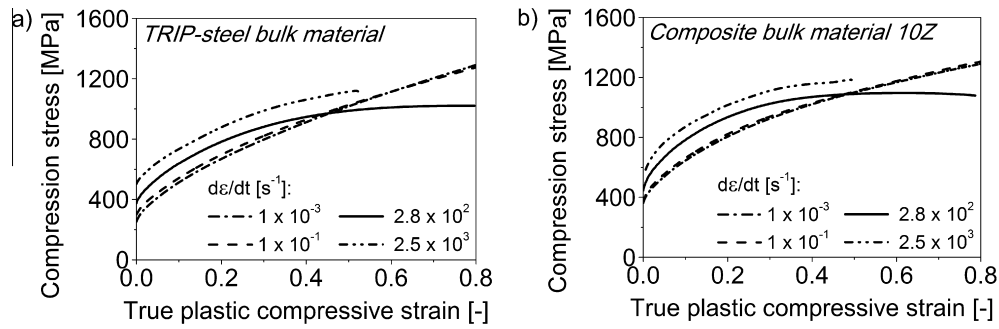| Material	Tensile yield stress $\sigma_{t,0.2\%}$ [MPa]	Ultimate tensile strength σ_u [MPa]	Tensile fracture elongationε_f [%]	Tensile tangent modulus E_t [GPa]	Proof stress $\sigma_{c,0.2\%}$ [MPa]	Stress at 40% $\sigma_{c,40\%}$ [MPa]	Micro-porosity p_m [%]
0Z	230 ± 7	510 ± 7	38.7 ± 2.0	2.70 ± 0.06	255 ± 1	1697 ± 19	8.6 ± 0.1
5Z	247 ± 9	464 ± 11	25.9 ± 0.1	2.22 ± 0.03	303 ± 13	1788 ± 35	7.8 ± 0.1
10Z	269 ± 4	429 ± 4	17.7 ± 0.5	1.64 ± 0.01	356 ± 8	1830 ± 1	6.7 ± 0.1

Fig. 5. Flow curves of two selected bulk materials under compressive loading depending on strain rate: (a) TRIP steel, (b) TRIP-matrix composite with 10 vol.% Mg-PSZ.

($E_t = (\sigma - \sigma_{2\%})/(\varepsilon - 0.02)$) decreased strongly with increasing zirconia particle fraction. The measured mechanical properties of the bulk materials for quasi-static tension and compression are listed in Table 4. The values of measured sinter microporosity (by Archimedes' method) are also included.

3.2. Strain-rate sensitivity of the bulk material

The flow stress of an austenitic high-alloyed TRIP steel rises with increasing strain rate due to the increased density of microstructural defects (viz. partial dislocations, stacking faults, etc.) and nucleation sites for α′-martensite formation. With regard to the honeycomb's steel matrix, a small degree of strengthening and deformability could be attributed to the formation of mechanical twins. According to previous findings (Decker et al., 2012; Krüger et al., 2011), the flow curves of the TRIP steel (Fig. 5a) and composite bulk materials studied (here: condition 10Z, Fig. 5b) at strain rates of $\dot{\varepsilon} \geqslant 2 \times 10^2$ s^{-1} reveal a significant initial increase in true compression stress but, ultimately, a decrease in overall stress level. This material softening was due to quasi-adiabatic sample heating. No appreciable effect on stress–strain response was observed at a medium strain rate of $\dot{\varepsilon} = 1 \times 10^{-1}$ s^{-1}.

The behavior of 0.2% proof stress $\sigma_{y,d}$ as a function of strain rate could be described by the Cowper-Symonds "overstress power law". The measured linear increase in proof stress with rising Mg-PSZ content could be expressed by a multiplication factor for particle reinforcement. Hence, the power law can be written as follows:

$$\sigma_{y,d} = \sigma_{y,s}^m (1 + gV_f) \left[1 + \left(\frac{\dot{\varepsilon}}{D} \right)^{(1/p)} \right], \tag{3}$$

where $\sigma_{y,s}^m$ denotes an equivalent quasi-static yield stress of the TRIP steel, and the material constants D and p characterize the matrix strain-rate sensitivity. The effect of particle reinforcement is expressed by $(1 + gV_f)$. V_f defines the volume fraction and $g(f)$ an empirical correction factor including the geometrical dimensions and morphology of the zirconia particles. The best agreement of the model with the experimental results was obtained using $\sigma_{y,s}^m = 269$ MPa, $g = 2.47$, $D = 17 \times 10^3$ s^{-1}, and $p = 4.09$, corresponding to the applied nominal strain rate $\dot{\varepsilon}$ (Fig. 6).

3.3. Axial compressive response of the honeycomb structures

The quasi-static OOP stress–strain curves (strain = displacement/length) for honeycombs of different relative density and material condition are given in Fig. 7a and b. In order to compensate for fluctuations in microporosity, the measured compression

stress is normalized to the effective relative density of each specimen.

The mechanical responses of the square honeycombs to OOP axial loads were consistently characterized by a linear-elastic regime, a primary plastic deformation stage with an extensive continuous stress increase, and the transition to a maximum or compressive peak stress. The secondary stage beyond the peak stress revealed an initial stress decline and a more or less constant crush plateau. Finally, the honeycomb densified in association with a steep increase in stress.

An increasing volume content of Mg-PSZ (viz. 5Z and 10Z) was accompanied by strengthening in the primary stage, starting with plastic yielding of the cell wall matrix material (viz. first inflection point in compressive stress–strain curve).

Fig. 8 shows a sequence of deformed configurations of the 64 cpsi (2×2) TRIP-steel honeycomb. The first structure bifurcation involved local torsional buckling of the outer cell walls, and local cell wall buckling in the inner core (A). After exceeding the compressive peak stress, the cell walls lost their rigidity. Larger flange deflections and the formation of folds (B) caused the
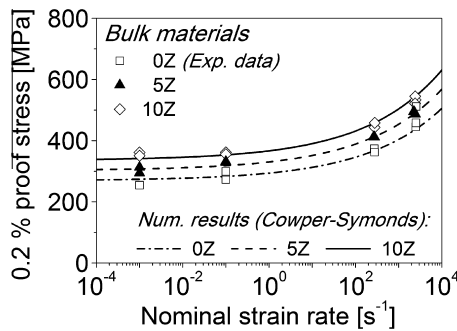
subsequent structural softening (see Fig. 7a). The continued plastic post-buckling collapse (C) and the contact of folds (D) induced high-order membrane deformations near the cell wall joints (cf. Wang et al., 2005) and in the collapsed surface regions. At the beginning of densification, the cross-sectional failure pattern exhibited twisted cell node elements that were constrained by each other (E).

In the high-density 196 cpsi (4×4) honeycombs, the initial local buckling of inner cell walls was partially replaced by a global plastic 'Euler-type' buckling mode (Fig. 9, A). These honeycombs were highly sensitive to shear deformation and friction effects by the test platens (B). Hence, they exhibited a symmetrical extensional collapse mode comparable with the barreling of cylindrical bulk specimens. The cell walls were highly compressed and generated plastic kinks with decreasing bending radii towards the center. The middle cruciform cell wall section was mostly governed by in-plane shear failure (C) or fracture (D) due to the constraints of the adjacent parts, which increased at higher deformation. The crushed specimen exhibited cross-sectional enlargement (E).

For the composite conditions, deformability and post-buckling strength were significantly reduced due to microscopic (Figs. 10a and b) and macroscopic damage events (Figs. 10c and d).

Similar results were obtained for the 64 cpsi (8×8) honeycombs and the 196 cpsi (14×14) specimens. The variation in cell number and sample size (with the same aspect ratio) had nearly no influence on the primary deformation stage and the compressive peak stress, but changed the cell wall constraints and interactions during post-buckling. Under quasi-static compression, the 196 cpsi honeycombs exhibited an average compressive peak stress of 400 MPa, which is approximately twice the maximum load of the lower-density 64 cpsi honeycombs (Fig. 11a, without stress normalization).

Common low-density metallic cellular structures ($\rho \leqslant 0.05$) were controlled by plastic post-buckling immediately after exceeding the yield stress of the bulk material. The high-density
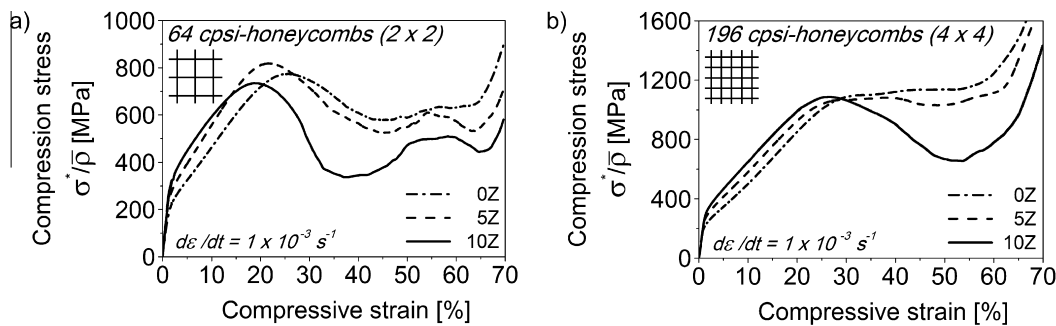

Fig. 6. Behavior of the 0.2% proof stress for the bulk materials as a function of strain rate comparing the experimental results and the model values of Eq. (3).

Fig. 7. Compressive stress–strain curves under quasi-static loading ($\dot{\varepsilon} = 1 \times 10^{-3}$ s^{-1}) depending on Mg-PSZ content and relative density: (a) 64 cpsi (2×2) honeycombs, $\bar{\rho} = 0.232 \pm 0.011$; (b) 196 cpsi ($4 \times 4$) honeycombs, $\bar{\rho} = 0.362 \pm 0.003$.
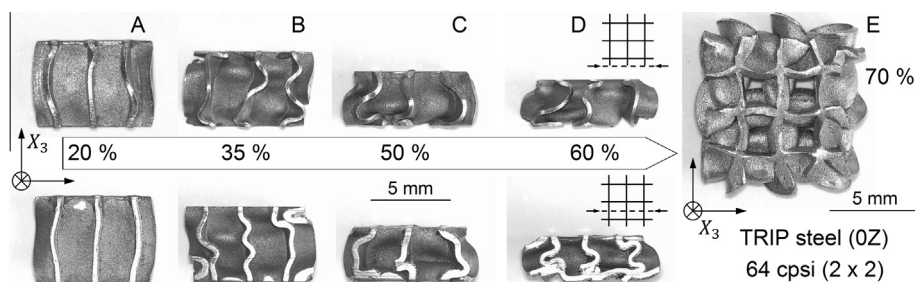

Fig. 8. Buckling and failure patterns of the 64 cpsi (2×2) -TRIP-steel honeycomb at different degrees of deformation under quasi-static OOP compression ($\dot{\varepsilon} = 1 \times 10^{-3}$ s^{-1}); side view of the outer shell above, longitudinal section of the inner core below (A–D); and a top view of a crushed specimen (E).
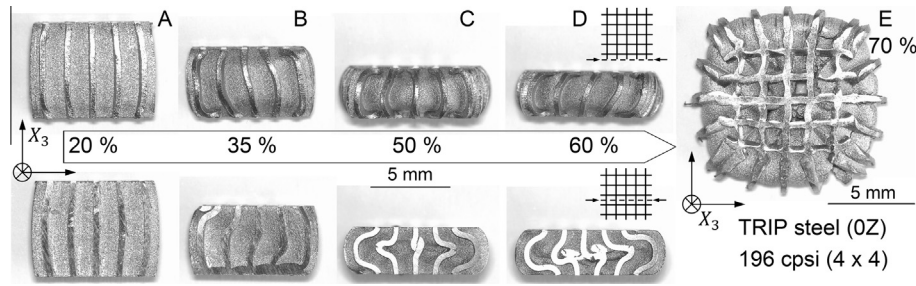
Fig. 9. Buckling and failure patterns of the 196 cpsi (4 × 4) -TRIP-steel honeycomb at different degrees of deformation under quasi-static OOP compression ($\dot{\varepsilon} = 1 \times 10^{-3}$ s^{-1}); side view of the outer shell above, longitudinal section of the inner core below (A–D); and a top view of a crushed specimen (E).
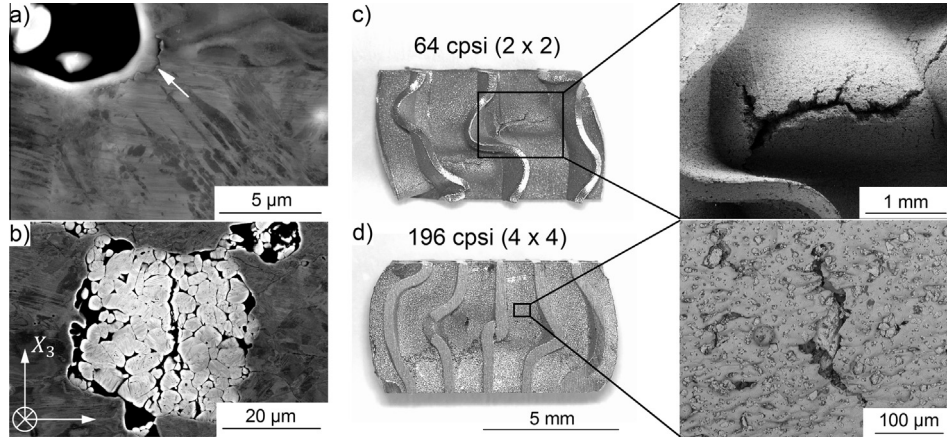

Fig. 10. Damage of tested composite honeycombs with 10 vol.% Mg-PSZ: (a) interface debonding and (b) fracture of ceramic clusters at 20% compressive deformation; cracks in (c) folds and (d) planar cell walls of different specimens at 35% compression.
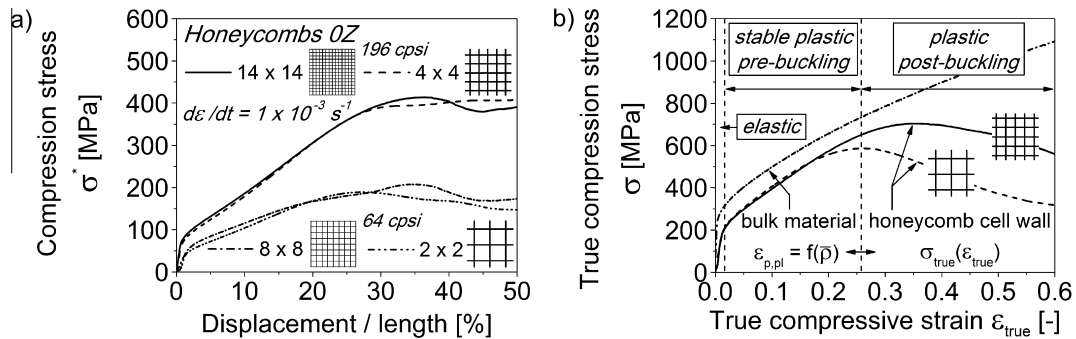

Fig. 11. (a) Mechanical responses of varied honeycomb specimens under quasi-static OOP compression ($\dot{\varepsilon} = 1 \times 10^{-3}$ s^{-1}); (b) comparison of the true compressive stress–strain responses of the honeycomb cell walls (196 and 64 cpsi) with the flow behavior of the bulk material; the results are given for the pure TRIP-steel condition.

TRIP-matrix honeycombs presented passed a stable plastic pre-buckling stage before achieving the post-buckling stage. The magnitudes of plastic failure strain $\varepsilon_{p,pl}$ (at load maximum) and compressive peak stress σ_p^* were dependent on relative density and the bulk material's strength and ductility. In general, their values were reduced with decreasing relative density and increasing degree of damage, triggered by a rising volume content of zirconia.

In accordance with the findings of Côté et al., (2004) on similar high-density steel honeycombs, the stretch-dominated plastic deformation of a single cell wall in the pre-buckling stage can be described by the uniaxial response of the bulk material. Small flange deflections are allowed. Therefore, the true compressive stress–strain behavior of the cell wall ($\sigma_{true}(\varepsilon_{true})$) is expressed by the following mechanical relationships:

$$\sigma_{true} = \frac{\sigma^*}{\bar{\rho}}(1 - \varepsilon) \tag{4}$$

and

$$\varepsilon_{true} = |\ln(1 - \varepsilon)|. \tag{5}$$

The pre-buckling responses of the representative honeycomb cell walls reflected the strain-hardening behavior of the corresponding TRIP-steel bulk material (Fig. 11b). However, the higher microporosity of the honeycombs weakened the cell walls and decreased the stress level.

By using the energy efficiency method (Tan et al., 2005a), the mean crushing stress σ_m^* and the plateau stress σ_{post}^* of each material and test condition were determined. First of all, the densification strain ε_d was calculated at the maximum of the energy efficiency coefficient $\eta(\varepsilon)$ as follows:

$$\eta(\varepsilon) = \frac{1}{\sigma^*(\varepsilon)} \int_0^\varepsilon \sigma^*(\varepsilon) d\varepsilon. \tag{6}$$
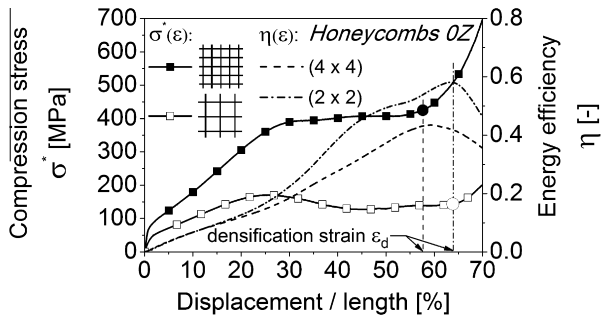
Fig. 12. Energy efficiency η of two TRIP-steel honeycombs of different relative density in correlation with their stress–strain curves under quasi-static OOP compression ($\dot{\varepsilon} = 1 \times 10^{-3}$ s^{-1}); the determination of densification strain ε_d is also illustrated.

Table 5
Properties of the honeycombs under quasi-static OOP compressive loading ($\dot{\varepsilon} = 1 \times 10^{-3}$ s^{-1}) depending on relative density and material condition.

Material condition	$\bar{\rho}$ [-]	σ_p^* [MPa]	$\sigma_p^*/\bar{\rho}$ [MPa]	σ_{post}^* [MPa]	$\sigma_{post}^*/\bar{\rho}$ [MPa]	$\sigma_m^*/\bar{\rho}$ [MPa]	ε_d [%]
0Z	0.226	177	783	152	673	629	63.5
	0.344	377	1095	383	1114	845	57.2
5Z	0.242	201	830	130	537	596	60.6
	0.367	406	1105	384	1044	890	57.8
10Z	0.236	174	729	108	457	483	66.6
	0.366	397	1086	309	843	828	59.8

After differentiation with respect to ε, Eq. (6) provides the beginning of structure densification

$$\left.\frac{\partial \eta(\varepsilon)}{\partial \varepsilon}\right|_{\varepsilon_d} = 0. \tag{7}$$

The mean crushing stress and the post-buckling (plateau) stress of the honeycombs are given as follows:

$$\sigma_m^* = \frac{1}{\varepsilon_d} \int_0^{\varepsilon_d} \sigma^*(\varepsilon) d\varepsilon \ and \ \sigma_{post}^* = \frac{1}{(\varepsilon_d - \varepsilon_0)} \int_{\varepsilon_0}^{\varepsilon_d} \sigma^*(\varepsilon) d\varepsilon, \tag{8}$$

where ε_0 defines the beginning of the plateau region at minimum load, assuming a constant value of $\varepsilon_0 = 0.4$ for all conditions.

As shown in Fig. 12, the energy efficiency during post-buckling of the 64 cpsi honeycombs was significantly higher than that of the 196 cpsi honeycombs. The more continuous deformation and extended plateau region of the lower-density structures contributes to their crashworthiness.

The calculated crush parameters for quasi-static OOP compression with respect to relative density and material condition are summarized in Table 5.
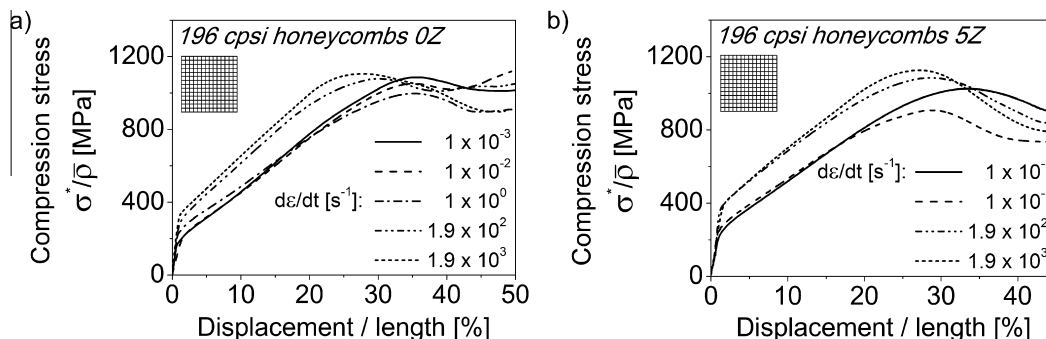
As expected, the specific mean crushing stress $\sigma_m^*/\bar{\rho}$ which describes the crush resistance of the honeycombs within the entire deformation range was generally not equal to the specific plateau stress $\sigma_{post}^*/\bar{\rho}$. The structure densification (ε_d) started at compressive strains of between 57% and 67%, whereby the higher relative density $\bar{\rho}$ of the 196 cpsi honeycombs was responsible for their lower crushing distance as compared with the 64 cpsi specimens. The highest values for compressive peak stress were obtained for the composite condition with 5 vol.% Mg-PSZ. However, the TRIP-steel specimens revealed the highest plateau stresses.

3.4. Strain-rate sensitivity of the honeycomb structures

The mechanical response of the TRIP steel and TRIP-matrix composite honeycombs under medium ($\dot{\varepsilon} = 10^{-1} \ldots 10^0$ s^{-1}) and dynamic OOP compression ($\dot{\varepsilon} = 1.9 \times 10^2 \ldots 1.9 \times 10^3$ s^{-1}) is controlled in particular by the inherent strain-rate sensitivity of the bulk material (Ehinger et al., 2011 2012b; Krüger et al., 2010).

Increasing strain rates cause high initial concentrations of microstructural defects in the steel matrix and larger distortions near the particle interfaces. Hence, the dynamic compression stress increased with respect to quasi-static loading up to a certain degree of deformation (Fig. 13a and b). However, further plastic deformation at medium strain rates was accompanied by a significant decline of strain hardening and stress level. As a consequence, the mechanical responses of the TRIP-steel and composite 196 cpsi honeycombs dropped below their quasi-static stress–strain curves. This decrease in the honeycomb's crush resistance was the result of material softening processes induced by quasi-adiabatic sample heating, similar to the process in the bulk material. High deformation temperatures promote the mobility and annihilation of dislocations and reduce the probability for strain-induced α'-martensite nucleation in the steel matrix (Ehinger et al., 2012b). Therefore, the strengthening associated with the TRIP effect was inhibited. By contrast, the honeycombs revealed a continuous increase in pre-buckling stress under dynamic impact loading ($\dot{\varepsilon} \geqslant 1.9 \times 10^2$ s^{-1}). Due to the shorter test time (a few number of ms or μs) and the high accumulation rate of microstructural defects, the material softening was less effective and shifted to higher deformation degrees. Accordingly, the quasi-adiabatic heating effect (maximum temperature gradient ~80 K) was compensated by dynamic strengthening. Local stress concentrations and an inhomogeneous strain or strain-rate distribution near particle interfaces provide an additional contribution of strength (Hong et al., 1993).

The interplay of deformation and damage mechanisms in the cell walls caused a nonlinear strain-rate dependence of specific compressive peak stress $\sigma_p^*/\bar{\rho}$ and plastic failure strain $\varepsilon_{p,pl}$ (Fig. 14). Maximum values were determined under quasi-static (nearly isothermal, $\dot{\varepsilon} = 10^{-3}$ s^{-1}) and dynamic impact loading ($\dot{\varepsilon} = 1.9 \times 10^2 \ldots 1.9 \times 10^3$ s^{-1}).

Fig. 13. Mechanical behavior of the 196 cpsi honeycombs under OOP compression at different strain rates: (a) TRIP-steel condition, (b) TRIP-matrix composite material with 10 vol.% Mg-PSZ.
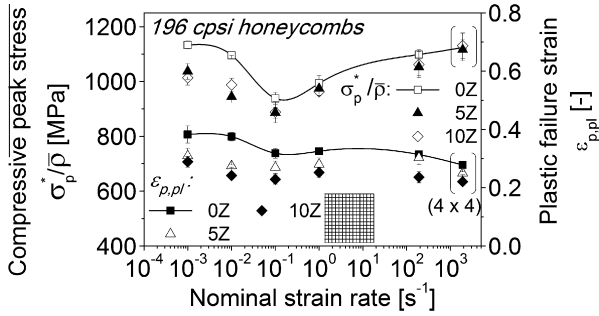
Fig. 14. Compressive peak stress and plastic failure strain of the 196 cpsi honeycombs (different material conditions) as functions of nominal strain rate.
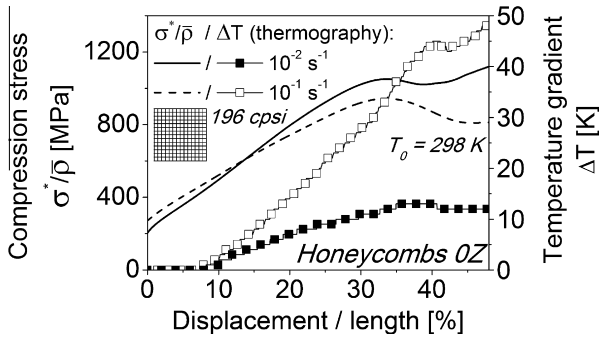

Fig. 15. Plastic compressive stress–strain response and measured increase in temperature of the TRIP steel 196 cpsi (14×14) honeycomb at quasi-static $(\dot{\varepsilon} = 10^{-2}\,\mathrm{s}^{-1})$ and medium strain rates $(\dot{\varepsilon} = 10^{-1}\,\mathrm{s}^{-1})$.

Previous microstructural investigations (Ehinger et al., 2012b) have proven that the evolution of the ferromagnetic α'-martensite phase fraction correlates with the strain-rate anomaly that is characteristic of material's strength and ductility. In the case of the bulk specimens, decreased strain hardening and stress saturation due to material softening were noticed first at higher strain rates $\dot{\varepsilon} \geqslant 2.8 \times 10^2\,\mathrm{s}^{-1}$ and higher compressive strains (see Fig. 5).

Fig. 15 shows the changes of temperature gradient ΔT during plastic deformation as measured by infrared thermography. Two different strain rates were considered.

The deformation temperature increased continuously in the stable pre-buckling stage. When exceeding the load maximum, a nearly constant temperature level was reached. Hence, the plastic work performed during material strain hardening was more temperature-sensitive than the post-buckling collapse of cell walls. Quasi-static OOP compression at $10^{-2}\,\mathrm{s}^{-1}$ caused a temperature increase of less than 13 K. However, a rise in strain rate by only one degree of magnitude results in a temperature change of $\Delta T = 30\ldots40\,\mathrm{K}$ as measured at the transition between pre-buckling and post-buckling response. Therefore, the driving force for α'-martensite formation (the TRIP effect) in the steel matrix is reduced, and twinning or dislocation glide mechanisms become more probable (Ehinger et al., 2011, 2012b).

According to the stress–strain relationships of Eqs. (4) and (5), the plastic deformation energy ΔW and the work hardening rate $\Theta^*/\bar{\rho}$ of the cell wall bulk material during stable compression in the pre-buckling stage (ε_{pl} = plastic compressive strain) were calculated.

$$\Delta W(\varepsilon_{pl}) = \int_0^{\varepsilon_{p,pl}} \sigma_{true}(\varepsilon_{pl})\,d\varepsilon_{pl} \tag{9}$$

and

$$\Theta^*/\bar{\rho} = \Delta\sigma_{true}/\Delta\varepsilon_{pl}. \tag{10}$$
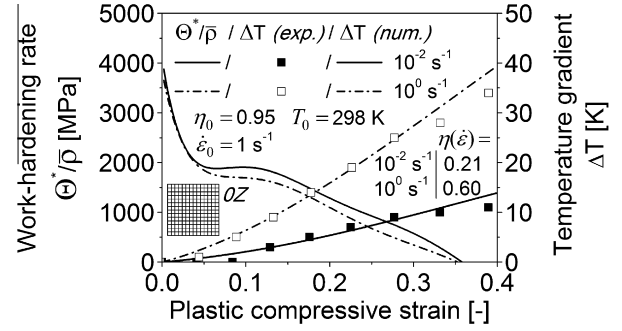

Fig. 16. Correlation of the measured and calculated temperature gradient with the work-hardening behavior of the TRIP-steel 196 cpsi honeycomb cell walls under OOP compression at quasi-static ($\dot{\varepsilon} = 10^{-2}\,\mathrm{s}^{-1}$) and medium strain rate ($\dot{\varepsilon} = 10^0\,\mathrm{s}^{-1}$).

Based on the results of Eq. (9) and the knowledge of specific heat capacity c_v and density ρ_s of the bulk material, the temperature gradient can be predicted theoretically.

$$\Delta T = \frac{\eta^*(\dot{\varepsilon})}{\rho_s c_v}\Delta W(\varepsilon_{pl}) \text{ with} \tag{11}$$

$$\eta^*(\dot{\varepsilon}) = \eta_0^*\lfloor 1 - \exp(-(p\dot{\varepsilon}^*)^q)\rfloor \text{ and } \dot{\varepsilon}^* = \dot{\varepsilon}/\dot{\varepsilon}_0 \tag{12}$$

The coefficient $\eta^*(\dot{\varepsilon})$ describes the quantity of saved thermal energy as a function of strain rate, including the parameters $p = 1$ and $q = 0.3$ and the reference strain rate $\dot{\varepsilon}_0 = 1\,\mathrm{s}^{-1}$, as well as the Taylor–Quinney factor $\eta_0^* = 0.95$. The latter is reached for strain rates of $\dot{\varepsilon} \geqslant 10^2\,\mathrm{s}^{-1}$ (Meyer et al., 2007).

A specific heat capacity of $c_v = 500\,\mathrm{J\,(kg\,K)}^{-1}$ and a bulk density of $6.61\,\mathrm{g\,cm}^{-3}$ (lowered by microporosity) were used for the calculation. The temperature gradients for two strain rates ($\dot{\varepsilon} = 10^{-2}\,\mathrm{s}^{-1}$ and $10^0\,\mathrm{s}^{-1}$) were determined and compared with the recorded temperature data of the TRIP-steel 196 cpsi honeycombs. Fig. 16 demonstrates the temperature effect on the work-hardening rate of the cell wall bulk material as a function of plastic compressive strain (only for pre-buckling).

The work-hardening rate reflected a gradual transition from material to structural behavior. Initial extrema indicated the martensitic phase transformation (TRIP effect) in the steel matrix. The parameter $\Theta^*/\bar{\rho}$ decreased sharply and finally reached zero at a plastic failure strain of $\varepsilon_{p,pl} \approx 0.35$ (viz. point of load maximum).

For all specimens, the predicted exponential increase in deformation temperature agreed very well with the in situ measurements in the pre-buckling stage of the honeycombs. As expected, first deviations between theoretical and experimental results occurred with the beginning of post-buckling. The pronounced sample heating at a medium strain rate of $\dot{\varepsilon} = 10^0\,\mathrm{s}^{-1}$ shifted the work-hardening rate to lower values compared to quasi-static loading.

Moreover, the localization of plastic deformation associated with the generation of stress and strain concentrations can also induce very inhomogeneous collapse modes in the honeycombs (Ehinger et al., 2012b). As already known from the literature (Baker et al., 1998; Lu and Hinnerichs, 2001; McFarland, 1963) transverse splitting and macro-shear are two frequently-occurring types.

In the present study, macro-shear band formation was mainly observed in the composite honeycombs at higher strain rates and higher deformation. The failure process was triggered by interface debonding, clustering, and rearrangement of zirconia particles. Fig. 17a and b demonstrate the mechanical response and (maximum) heating of a 196 cpsi honeycomb with 10 vol.% Mg-PSZ affected by macro-shear failure.

The strain localization had already begun in the pre-buckling stage of the sample, and was indicated by a disproportionately high increase in deformation temperature (Fig. 17a). Starting from the
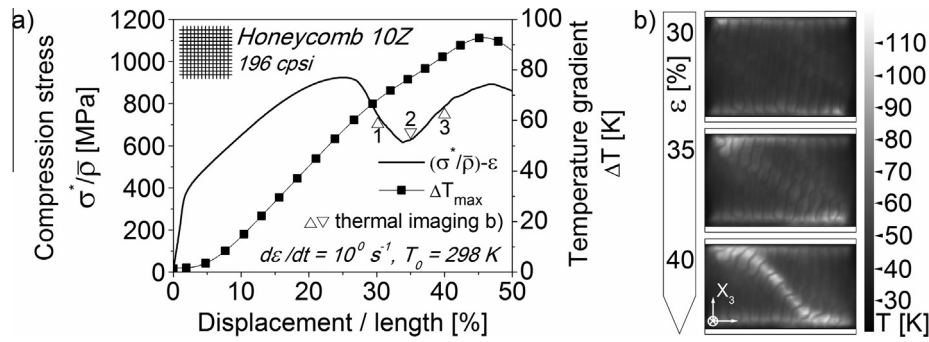
Fig. 17. (a) Compression stress and temperature gradient of a composite (10Z) 196 cpsi honeycomb (without outer skin) at medium strain rate ($\dot{\varepsilon} = 10^0\,\text{s}^{-1}$) as a function of deformation; (b) in situ thermography recording the behavior at the beginning of post-buckling.
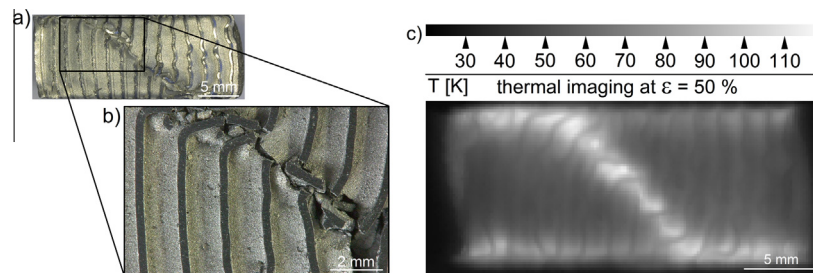

Fig. 18. (a) and (b) Collapse patterns of the composite (10Z) 196 cpsi honeycomb at 50% deformation under OOP compression at a medium strain rate ($\dot{\varepsilon} = 10^0\,\text{s}^{-1}$); (c) corresponding thermal image.

loaded edges, the shear band propagated diagonally towards the center of the cellular frame (Fig. 17b), separating the honeycomb into two parts (Fig. 18a). The collapsed cell wall sections were dominated by macro-cracking and fragmentation (Fig. 18b). Therefore, the post-buckling stress decreased. The maximum temperature gradient within the shear region was 95 K. The rest of the cell walls remained straight without visible damage sites, revealing a homogeneous temperature field in the range of 40–60 K (Fig. 18c).

Neither an inertial stabilization of the honeycomb webs against buckling nor a strengthening effect due to fluid compression or shock wave propagation were observed in this study.

4. Conclusions

The mechanical and structural response of high-density TRIP steel and TRIP-matrix composite square honeycombs was investigated under axial compression in the out-of-plane loading direction. Differences in relative density, Mg-PSZ content, and strain rate affected their properties and deformation mechanisms. The stress–strain behavior of the honeycombs was characterized by a linear-elastic regime and pre-buckling and post-buckling stages, followed by a structural densification. During pre-buckling, the structures underwent a primary stable plastic deformation associated with a continuous increase in compression stress like the bulk material. The honeycomb cell walls were subjected to axial crushing that was finally accompanied by local or torsional buckling and global 'Euler-type' buckling mechanisms. Global buckling was more pronounced in the higher-density 196 cpsi honeycombs due to larger geometric constraints and friction effects. When exceeding the maximum loading limit (compressive peak stress), a transition from the stable to a secondary unstable plastic deformation occurred. While the post-buckling of the 64 cpsi honeycombs was characterized by folding collapse, the 196 cpsi specimens failed in a symmetric extensional collapse mode with plastic kink formation.

The initial compression stress level of the honeycombs rose with increasing Mg-PSZ content and strain rate. Continued

compression induced damage processes (especially in the composite variants) and higher deformation temperatures in the cell wall material. The compressive peak stress and the plastic failure strain of the 196 cpsi honeycombs exhibited a strain-rate anomaly. This could be explained by the effect of quasi-adiabatic sample heating at $\dot{\varepsilon} \geqslant 10^{-2}\,\text{s}^{-1}$ and by the damage evolution. The measured and numerically confirmed increase in deformation temperature was responsible for the pronounced material softening at medium strain rates. Furthermore, macro-shear failure associated with high strain and temperature concentrations also caused the significant decline of the honeycomb's crush resistance.

The present study provides information about the characteristics of high-density TRIP steel and TRIP-matrix composite square honeycombs and their potential for future applications. These results are not comparable with previous findings on low-density cellular structures.

References

Alghamdi, A.A.A., 2001. Collapsible impact energy absorbers: an overview. Thin-Walled Struct. 39, 189–213.

Aneziris, C.G., Schärfl, W., Biermann, H., Martin, U., 2009. Energy-absorbing TRIP-steel/Mg-PSZ composite honeycomb structures based on ceramic extrusion at room temperature. Int. J. Appl. Ceram. Technol. 6, 727–735.

Baker, W.E., Togami, T.C., Weydert, J.C., 1998. Static and dynamic properties of high-density metal honeycombs. Int. J. Impact Eng. 21, 149–163.

Barnes, A.T., Ravi-Chandar, K., Kyriakides, S., Gaitanaros, S., 2014. Dynamic crushing of aluminum foams: part I – experiments. Int. J. Solids Struct. 51, 1631–1645.

Côté, F., Deshpande, V.S., Fleck, N.A., Evans, A.G., 2004. The out-of-plane compressive behavior of metallic honeycombs. Mater. Sci. Eng., A 380, 272–280.

Côté, F., Deshpande, V.S., Fleck, N.A., Evans, A.G., 2006. The compressive and shear responses of corrugated and diamond lattice materials. Int. J. Solids Struct. 43, 6220–6242.

Decker, S., Krüger, L., Richter, S., Martin, S., Martin, U., 2012. Strain-rate-dependent flow stress and failure of an Mg-PSZ reinforced TRIP matrix composite produced by spark plasma sintering. Steel Res. Int. 83, 521–528.

Dharmasena, K.P., Wadley, H.N.G., Xue, Z., Hutchinson, J.W., 2008. Mechanical response of metallic honeycomb sandwich panel structures to high-intensity dynamic loading. Int. J. Impact Eng. 35, 1063–1074.

Ehinger, D., Krüger, L., Krause, S., Martin, U., Weigelt, C., Aneziris, C.G., 2012a. Dynamic impact of high-density square honeycombs made of TRIP steel and TRIP matrix composite material. In: 10th International Conference on the Mechanical and Physical Behaviour of Materials under Dynamic Loading (DYMAT), EPJ WEB of Conf. 26, 1–6.

Ehinger, D., Krüger, L., Martin, U., Weigelt, C., Aneziris, C.G., 2011. Strain rate effect on material behavior of TRIP-steel/zirconia honeycomb structures. Steel Res. Int. 82, 1048–1056.

Ehinger, D., Krüger, L., Martin, U., Weigelt, C., Aneziris, C.G., 2012b. Deformation mechanisms and martensitic phase transformation in TRIP-steel/zirconia honeycombs. Steel Res. Int. 83, 565–575.

Elnasri, I., Pattofatto, S., Zhao, H., Tsitsiris, H., Hild, F., Girard, Y., 2007. Shock enhancement of cellular structures under impact loading: part I experiments. J. Mech. Phys. Solids 55, 2652–2671.

Foo, C.C., Chai, G.B., Seah, L.K., 2007. Mechanical properties of Nomex material and Nomex honeycomb structure. Compos. Struct. 80, 588–594.

Gaitanaros, S., Kyriakides, S., 2014. Dynamic crushing of aluminum foams: part II – analysis. Int. J. Solids Struct. 51, 1646–1661.

Gent, A.N., Thomas, A.G., 1963. Mechanics of foamed elastic materials. Rubber Chem. Tech. 36, 597–610.

Gibson, L.J., Ashby, M.F., 1997. Cellular Solids – Structure & Properties. Cambridge University Press, Cambridge.

Goldsmith, W., Louie, D.L., 1995. Axial perforation of aluminium honeycombs by projectiles. Int. J. Solids Struct. 32, 1017–1046.

Gong, L., Kyriakides, S., 2005. Compressive response of open cell foams part II: initiation and evolution of crushing. Int. J. Solids Struct. 42, 1381–1399.

Gong, L., Kyriakides, S., Jang, W.-Y., 2005. Compressive response of open-cell foams. Part I: morphology and elastic properties. Int. J. Solids Struct. 42, 1355–1379.

Heimbs, S., Schmeer, S., Middendorf, P., Maier, M., 2007. Strain rate effects in phenolic composites and phenolic-impregnated honeycomb structures. Compos. Sci. Technol. 67, 2827–2837.

Hong, S.I., Gray III, G.T., Lewandowski, J.J., 1993. Dynamic deformation behavior of Al–Zn–Mg–Cu alloy matrix composites reinforced with 20 vol.% SiC. Acta Metall. Mater. 41, 2337–2351.

Jang, W.-Y., Kyriakides, S., 2009a. On the crushing of aluminum open-cell foams: part I. Exp. Int. J. Solids Struct. 46, 617–634.

Jang, W.-Y., Kyriakides, S., 2009b. On the crushing of aluminum open-cell foams: part II analysis. Int. J. Solids Struct. 46, 635–650.

Klintworth, J.W., Stronge, W.J., 1988. Elasto-plastic yield limits and deformation laws for transversely crushed honeycombs. Int. J. Mech. Sci. 30, 273–292.

Klintworth, J.W., Stronge, W.J., 1989. Plane punch indentation of a ductile honeycomb. Int. J. Mech. Sci. 31, 359–378.

Krüger, L., Decker, S., Ohser-Wiedemann, R., Ehinger, D., Martin, S., Martin, U., Seifert, H.J., 2011. Strength and failure behaviour of spark plasma sintered steel-zirconia composites under compressive loading. Steel Res. Int. 82, 1017–1021.

Krüger, L., Ehinger, D., Martin, U., Martin, S., Weigelt, C., Aneziris, C.G., 2010. Microstructure and mechanical properties of cold extruded, cellular TRIP-matrix composite structures under quasi-static and dynamic compression. High Performance Struct. Mater. V, WIT Trans. Built Environ. 112, 39–49.

López Jiménez, F., Triantafyllidis, N., 2013. Buckling of rectangular and hexagonal honeycomb under combined axial compression and transverse shear. Int. J. Solids Struct. 50, 3934–3946.

Lu, W.-Y., Hinnerichs, T., 2001. Crush of high density aluminum honeycombs. In: ASME International Mechanical Engineering Congress and Exposition (IMECE'01), AMD-25453, New York, NY, USA, November 11–16, 2001. pp. 203–211.

Martin, S., Richter, S., Decker, S., Martin, U., Krüger, L., Rafaja, D., 2011. Reinforcing mechanism of Mg-PSZ particles in highly-alloyed TRIP steel. Steel Res. Int. 82, 1133–1140.

McFarland, R.K., 1963. Hexagonal cell structures under post-buckling axial load. Am. Inst. Aeron. Astron. (AIAA) J. 1, 1380–1385.

Meyer, L.W., Herzig, N., Halle, T., Hahn, F., Krüger, L., Staudhammer, K.P., 2007. A basic approach for strain rate dependent energy conversion including heat transfer effects: an experimental and numerical study. J. Mater. Proc. Technol. 182, 319–326.

Mohr, D., Doyoyo, M., 2003. Nucleation and propagation of plastic collapse bands in aluminum honeycomb. J. Appl. Phys. 94, 2262–2270.

Mohr, D., Doyoyo, M., 2004. Large plastic deformation of metallic honeycomb: orthotropic rate-independent constitutive model. Int. J. Solids Struct. 41, 4435–4456.

Papka, S.D., Kyriakides, S., 1994. In-plane compressive response and crushing of honeycomb. J. Mech. Phys. Solids 42, 1499–1532.

Papka, S.D., Kyriakides, S., 1998a. Experiments and full-scale numerical simulations of in-plane crushing of a honeycomb. Acta Mater. 46, 2765–2776.

Papka, S.D., Kyriakides, S., 1998b. In-plane crushing of a polycarbonate honeycomb. Int. J. Solids Struct. 35, 239–267.

Patel, M.R., Finnie, I., 1970. Structural features and mechanical properties of rigid cellular plastics. J. Mater. 5, 909–932.

Pattofatto, S., Elnasri, I., Zhao, H., Tsitsiris, H., Hild, F., Girard, Y., 2007. Shock enhancement of cellular structures under impact loading: part II analysis. J. Mech. Phys. Solids 55, 2672–2686.

Prakash, O., Bichebois, P., Brechet, Y., Louchet, F., Embury, J.D., 1996. A note on the deformation behaviour of two-dimensional model cellular structures. Philos. Mag. A 73, 739–751.

Radford, D.D., McShane, G.J., Deshpande, V.S., Fleck, N.A., 2007. Dynamic compressive response of stainless-steel square honeycombs. ASME 74, 658–667.

Rathbun, H.J., Radford, D.D., Xue, Z., He, M.Y., Yang, J., Deshpande, V.S., Fleck, N.A., Hutchinson, J.W., Zok, F.W., Evans, A.G., 2006. Performance of metallic honeycomb-core sandwich beams under shock loading. Int. J. Solids Struct. 43, 1746–1763.

Reid, S.R., Peng, C., 1997. Dynamic uniaxial crushing of wood. Int. J. Impact Eng. 19, 531–570.

Shaw, M.C., Sata, T., 1966. The plastic behavior of cellular materials. Int. J. Mech. Sci. 8, 469–478.

Shim, V.P.-W., Stronge, W.J., 1986. Lateral crushing in tightly packed arrays of thin-walled metal tubes. Int. J. Mech. Sci. 28, 709–728.

Tan, P.J., Reid, S.R., Harrigan, J.J., Zou, Z., Li, S., 2005a. Dynamic compressive strength properties of aluminium foams. Part I – experimental data and observations. J. Mech. Phys. Solids 53, 2174–2205.

Tan, P.J., Reid, S.R., Harrigan, J.J., Zou, Z., Li, S., 2005b. Dynamic compressive strength properties of aluminium foams. Part II – 'shock' theory and comparison with experimental data and numerical models. J. Mech. Phys. Solids 53, 2206–2230.

Triantafyllidis, N., Schraad, M.W., 1998. Onset of failure in aluminum honeycombs under general in-plane loading. J. Mech. Phys. Solids 46, 1089–1124.

Wadley, H.N.G., Dharmasena, K.P., Queheillalt, D.T., Chen, Y., Dudt, P., Knight, D., Kiddy, K., Xue, Z., Vaziri, A., 2007. Dynamic compression of square honeycomb structures during underwater impulsive loading. J. Mater. Mech. Struct. 2, 2025–2048.

Wang, A.-J., Kumar, R.S., McDowell, D.L., 2005. Mechanical behavior of extruded prismatic cellular metals. Mech. Adv. Mater. Struct. 12, 185–200.

Warren, W.E., Kraynik, A.M., 1987. Foam mechanics: the linear elastic response of two-dimensional spatially periodic cellular materials. Mech. Mater. 6, 27–37.

Weigelt, C., Aneziris, C.G., Yanina, A., Guk, S., 2011. Ceramic processing for TRIP-steel/Mg-PSZ composite materials for mechanical applications. Steel Res. Int. 82, 1080–1086.

Wierzbicki, T., 1983. Crushing analysis of metal honeycombs. Int. J. Impact Eng. 1, 157–174.

Wilbert, A., Jang, W.-Y., Kyriakides, S., Floccari, J.F., 2011. Buckling and progressive crushing of laterally loaded honeycomb. Int. J. Solid Struct. 48, 803–816.

Yamashita, M., Gotoh, M., 2005. Impact behavior of honeycomb structures with various cell specifications – numerical simulation and experiment. Int. J. Impact Eng. 32, 618–630.

Zhang, J., Ashby, M.F., 1992. The out-of-plane properties of honeycombs Int. J. Mech. Sci. 34, 475–489.

Zhao, H., Abdennadher, S., 2004. On the strength enhancement under impact loading of square tubes made from rate insensitive metals. Int. J. Solids Struct. 41, 6677–6697.

Zhao, H., Elnasri, I., Abdennadher, S., 2005. An experimental study on the behaviour under impact loading of metallic cellular materials. Int. J. Mech. Sci. 47, 757–774.

Zhao, H., Gary, G., 1998. Crushing behaviour of aluminium honeycombs under impact loading. Int. J. Impact Eng. 21, 827–836.

Zhou, Q., Mayer, R.R., 2002. Characterization of aluminium honeycomb material failure in large deformation compression, shear, and tearing. J. Eng. Mater. Technol. 124, 412–420.